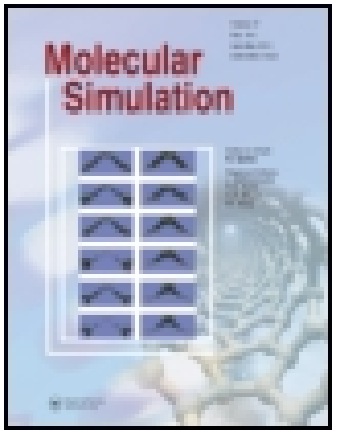

Molecular Simulation
Publication details, including instructions for authors and subscription information:
http://www.tandfonline.com/loi/gmos20

Vapour-liquid phase equilibria of simple fluids confined in patterned slit pores

Sudhir K. Singh [a] , Sandip Khan [a] , Subimal Jana [a] & Jayant K. Singh [a]
[a] Department of Chemical Engineering , Indian Institute of Technology , Kanpur, 208016, India
Published online: 01 Dec 2010.

To cite this article: Sudhir K. Singh , Sandip Khan , Subimal Jana & Jayant K. Singh (2011) Vapour-liquid phase equilibria of simple fluids confined in patterned slit pores, Molecular Simulation, 37:05, 350-360

To link to this article: http://dx.doi.org/10.1080/08927022.2010.514778

Molecular Simulation
Vol. 37, No. 5, April 2011, 350–360

Taylor & Francis
Taylor & Francis Group

Vapour–liquid phase equilibria of simple fluids confined in patterned slit pores

Sudhir K. Singh, Sandip Khan, Subimal Jana and Jayant K. Singh*

Department of Chemical Engineering, Indian Institute of Technology, Kanpur 208016, India

(*Received 15 December 2009; final version received 1 February 2010*)

We present the influence of surface heterogeneity on the vapour–liquid phase behaviour of square-well fluids in slit pores using grand-canonical transition-matrix Monte Carlo simulations along with the histogram-reweighting method. Properties such as phase coexistence envelopes, critical properties and local density profiles of the confined SW fluid are reported for chemically and physically patterned slit surfaces. It is observed that in the chemically patterned pores, fluid–fluid and surface attraction parameters along with the width of attractive and inert stripes play fundamentally different roles in the phase coexistence and critical properties. On the other hand, pillar gap and height significantly affect the vapour–liquid equilibria in the physically patterned slit pores. We also present the effect of chemically and physically patterned slit surfaces on the spreading pressure.

Keywords: phase equilibria; confined fluids; Monte Carlo

1. Introduction

Technological advances in recent years have made it possible to imprint solid surfaces with well-defined physical and chemical structures. A practical and feasible 'lab-on-a-chip', i.e. micro/nanoscale lab, requires an appropriate design based on compatible surfaces for a specific process on a nanometre length scale. These micro/nanoscale labs should have some basic properties similar to macroscopic labs, e.g. test tubes in macroscopic laboratories. It should have a well-defined geometry by which one can measure the precise amount of fluid contained in them; it should be able to confine variable amounts of fluid and it should be accessible in such a way that one can add and extract fluid in a convenient manner. The simplest channel geometry that can be used in this way corresponds to channels with a rectangular cross-section. The width and depth of these channels can be varied between a few nanometres and a couple of micrometres. These patterns can be created on rather different length scales by different experimental techniques [1–8]. If such a patterned surface is in contact with a fluid, the corresponding interface has a position-dependent free energy, which reflects the underlying surface pattern. As a result, the surface pattern will modulate the shape of the fluid layer and thus will affect its morphology. Important applications of these structures are in micro-fluidics and in advance separation technologies.These patterned surfaces enable one to control the microscopic flow of liquids on designated chemical channels and to facilitate the fabrication of 'chemical chips' which may act as micro-laboratories for the investigation and processing of rare and valuable liquids [9,10].

Over the years, a large number of experiments have been carried out to study the adsorption of complex molecules on chemically heterogeneous substrates. Agheli et al. [11] investigated protein adsorption on hydrophilic substrates bearing regularly spaced hydrophobic nanopatterns. Lei et al. [12] examined the site-selective adsorption and the directional diffusion of a single molecule as well as the molecular clusters of copper phthalocyanine. Shi et al. [13] used chemically modified patterned surface as a good matrix for selective adsorption of polystyrene nanoparticles with both positive and negative charges. Recent advances in statistical mechanics and the rapid growth in computational power enabled theoretical and simulation studies of complex molecules adsorption on patterned surfaces. Patra and Linse [14] investigated the structural properties of polymer brushes adsorbed on nanopatterned surfaces. The results showed that the central part of a patterned brush remains nearly unchanged as long as the pattern is several times wider than the height of the brush. Recently, Striolo [15] explained how the presence of a solid hard mask, used to mimic nanoscale patterns on an underlying hydrophobic surface, affects surfactant adsorption. Chen et al. [16] investigated the recognition affinity of multiblock copolymers on nanopatterned surfaces using Monte Carlo molecular simulations. The authors examined different architectures of copolymers on a variety of patterned surfaces consisting of adsorbing and non-adsorbing stripes.

These investigations indicate that, in the nanoscopic length scale, the behaviour of fluids on physically or chemically patterned surfaces becomes more fascinating

*Corresponding author. Email: jayantks@iitk.ac.in

ISSN 0892-7022 print/ISSN 1029-0435 online

DOI: 10.1080/08927022.2010.514778
http://www.informaworld.com

and the observed phenomena are more complex as both surface and spatial inhomogeneity of the fluid becomes important. In all of the above-mentioned investigations, studies on the vapour–liquid phase equilibria, where both of the confining surfaces being decorated with chemical or physical patterns of periodic nature, are not addressed. Schoen and Diestler [17] concluded that in a chemically patterned slit pore when $2 < H < 5$ (where H is the slit width), a local vapour–liquid interface will form between strongly and weakly attractive stripes with the interface perpendicular to the slit surfaces. However, when H crosses a critical value, the long-range attraction of the strongly attractive stripes is effectively weakened. Hence, the liquid-like film can not only be sustained on the attractive stripes, instead would cover both strongly and weakly attractive stripes, and a vapour phase would form in the centre of the pore in equilibrium with the liquid film at the walls. Moreover, it was concluded that if the width of the weakly attractive stripe is sufficiently small as compared to the strongly attractive stripe, then the liquid-like film would persist even with larger H, and as a result local vapour–liquid interfaces could be seen between these strongly and weakly attractive stripes. Another investigation of the vapour–liquid phase equilibria using the molecular simulation technique, in a geometrically and a chemically disordered cylindrical pore, carried out by Puibasset [18] for a Lennard-Jones (LJ) fluid indicates that the chemical disorder has a much stronger effect as compared to the geometric disorder, on the phase diagram of the confined fluid. Moreover, investigations done by Puibasset [19,20] indicate that the chemical undulation is able to stabilise an intermediate phase, the so-called bridge phase between the vapour and liquid phases. Because of the stabilisation of the bridge-like phase, two apparent critical temperatures were reported. On the other hand, the geometric constriction is not able to stabilise this bridge phase.

However, investigations on the vapour–liquid phase equilibria in the patterned slit pore surfaces are rare and need a fresh look. In the current investigations, we have tried to find out the answers of a few simple questions, which remain unexplored until now. How does the effective attraction of the attractive stripe over inert stripe will modulate the vapour–liquid phase equilibria of the fluid of different attractive nature? How does the spreading pressure (pressure parallel to the slit surfaces) change with the patterned surfaces and fluid nature in the slit pores? To what extent do various critical properties change in chemically patterned slit surfaces with the change in effective attraction range of the attractive stripe and the fluid nature? What are the effects of pillar gap, width and height on the vapour–liquid phase equilibria and critical properties of simple fluids in physically patterned slit pores? The rest of the paper is organised as follows. Section 2 outlines the potential models and simulation details used in this work. The results obtained in this work are described in Section 3, and, finally, Section 4 presents the main conclusions.

2. Simulation details

Fluid properties under confinement can be studied primarily by GEMC [18,21] and GCMC [22–24]. In this work, we have employed grand-canonical transition-matrix Monte Carlo (GC-TMMC), which is described in detail elsewhere [25,26].

In this work, fluid–fluid interaction and attractive stripe wall–fluid interaction are represented by the square-well (SW) potentials and the hard-wall potential represents the inert stripe wall–fluid interaction:

$$u_{\mathrm{ff}}(r) = \begin{cases} \infty, & 0 < r < \sigma_{\mathrm{ff}} \\ -\varepsilon_{\mathrm{ff}}, & \sigma_{\mathrm{ff}} \le r < \lambda_{\mathrm{f}}\sigma_{\mathrm{ff}} \\ 0, & \lambda_{\mathrm{f}}\sigma_{\mathrm{ff}} \le r \end{cases}, \tag{1}$$

$$u_{\mathrm{wf}}(z) = \begin{cases} \infty, & 0 < z < \sigma_{\mathrm{ff}}/2 \\ -\varepsilon_{\mathrm{wf}}, & \sigma_{\mathrm{ff}}/2 \le z < \lambda_{\mathrm{w}}\sigma_{\mathrm{ff}} \\ 0, & \lambda_{\mathrm{w}}\sigma_{\mathrm{ff}} \le z \end{cases}, \tag{2}$$

where $\lambda\sigma$ is the potential-well diameter; ε is the depth of the well; and σ is the diameter of the hard core. We adopt units such that $\varepsilon_{\mathrm{ff}}$ and σ_{ff} are unity. So, normalised temperature is represented by T, density by ρ and pressure by P.

In this work, critical properties are estimated by using the phase coexistence data obtained via GC-TMMC and the least-squares fit of the following scaling law [27,28]:

$$\rho_{\mathrm{l}} - \rho_{\mathrm{v}} = C\left(1 - \frac{T}{T_{\mathrm{c}}}\right)^{\beta}, \tag{3}$$

where ρ_{l}, ρ_{v} and T_{c} are phase coexistence liquid and vapour number densities, and critical temperature, respectively; C and β are fitting parameters. The parameter β is also known as the critical exponent. The critical temperature, T_{c}, estimated from Equation (3) is used to calculate the critical density, ρ_{c}, from the least-squares fit of the following equation:

$$\frac{\rho_{\mathrm{l}} + \rho_{\mathrm{v}}}{2} = \rho_{\mathrm{c}} + D(T - T_{\mathrm{c}}), \tag{4}$$

where D is a fitting parameter.

The critical pressure, P_{c}, is calculated using the least-squares fit of the saturation pressure data obtained from the GC-TMMC simulations to the following expression, which has a similar form to the Antoine equation:

$$\ln P_{\mathrm{c}} = A - \frac{B}{T_{\mathrm{c}}}, \tag{5}$$

where A and B are fitting parameters. The above empirical form is also utilised to obtain the critical pressure for confined fluids as shown earlier for SW fluids [25] and alkanes [29].

The saturated density profiles (perpendicular and parallel to the slit surface), ρ_z and ρ_x are obtained by recording $\rho(N, z \text{ or } x)$ for each particle number sampled during GC-TMMC simulations. Phase coexistence density profiles are finally obtained using the following expression:

$$\rho(z \text{ or } x)_{\text{vapour/liquid}} = \frac{\sum_{i \in \text{vapour/liquid}} \Pi_C(i)\rho(i, z \text{ or } x)}{\sum_{i \in \text{vapour/liquid}} \Pi_C(i)}, \quad (6)$$

where Π_C is the phase coexistence probability density distribution obtained from the application of the histogram-reweighting technique [30] on the transition matrix data obtained from the GC-TMMC simulation.

GC-TMMC simulations are conducted with 30% displacement and 70% insertion/deletion moves. For the phase coexistence calculation, the box length (all lengths are given in units of the core diameter $\sigma_{ff} = 1$) was varied from $L \sim 8$ to 32 depending on the pillar height and pore width. Four independent runs are conducted to obtain the statistical error in coexisting densities and critical properties. The errors in critical temperature (T_c), critical density (ρ_c) and critical pressure (P_c) in the patterned slit geometries are less than 0.22, 0.14 and 0.36%, respectively.

3. Results and discussion

3.1 *Phase equilibria in chemically patterned pores*

It is a well-established fact that critical temperature decreases under confinement irrespective of the shape and nature of the pore, but critical density may decrease or increase depending on the surface–fluid interactions and extent of the confinement [31,32]. In this work, we studied the behaviour of phase coexistence and critical properties for SW fluids in confined geometries of three different natures, namely hard slit pore, chemically homogeneous attractive and heterogeneous slit pores comprised of inert and attractive stripes. Our investigations, as shown in Figure 1, indicate that phase coexistence density of the vapour and liquid phases increases as the effective interaction of the fluid molecules with the confining surfaces increases. Moreover, the effect of attraction on the liquid density branch is more pronounced, as compared to the vapour density branch. On the other hand, for the studied slit pore width, $H = 8$, critical temperature, T_c, remains almost unaffected, similar to that seen for the LJ fluid in the chemically patterned cylindrical pore [18], with the change in the nature of slit surfaces from chemically patterned to homogeneous attractive surfaces. However, critical density, ρ_c, increases as the effective

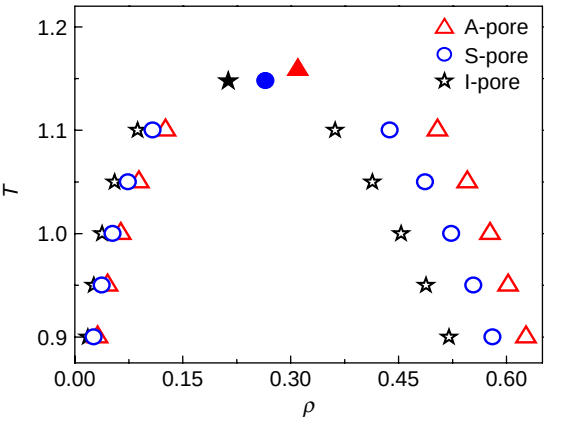

Figure 1. Vapour–liquid phase coexistence envelope of a SW fluid confined in homogeneous attractive (A), ordered stripe (S, stripe width $w = 2$ is used for both attractive and inert stripes) and hard-wall slit (I) pores with slit width $H = 8$. Filled symbols indicate critical points. Interaction parameters $\lambda_{ff} = 1.5$, $\varepsilon_{ff} = 1.0$, $\lambda_{wf} = 1.0$ and $\varepsilon_{wf} = 2.0$ are used. Error bars are of the order of the symbol size.

surface attraction increases from the patterned stripe to homogeneous attractive surfaces, which is contrary to the behaviour seen in the cylindrical pore [18].

It is well understood that the critical temperature of SW fluids increases with the increase in the fluid–fluid interaction range for both the bulk and the confined fluid. We observed a similar behaviour for the patterned slit pore cases as shown in Figure 2(a) for a fixed wall–fluid interaction, $\lambda_{wf} = 1.0$, $\varepsilon_{wf} = 2.0$, $\varepsilon_{ff} = 1.0$, $w = 2$ and $H = 8$. Interestingly, this behaviour is not observed for the critical density. Figure 2(a) shows that with the increase in λ_{ff}, from 1.5 to 2.5, critical temperature monotonically increases, but critical density first decreases to a minima and subsequently increases. This clearly suggests that the fluid interaction range has non-monotonic dependence on the critical densities in the patterned slit pore geometries. We also studied the effect of the wall–fluid interaction range, ε_{wf}, on phase coexistence and critical properties in the patterned slit pore surfaces. Unlike the λ_{ff}, the wall–fluid interaction range, λ_{wf}, plays a different role. In Figure 2(b) it is shown that at a lower surface attraction, $\varepsilon_{wf} = 2$, critical temperature is almost constant for the $\lambda_{wf} =$ 1.0–1.5 range. A subsequent increase in λ_{wf} decreases the critical temperature. On the other hand, critical density monotonically increases with the increase in λ_{wf}. Significant lowering of critical temperature at higher λ_{wf} is attributed to the shifting of the vapour density branch towards higher values and insignificant change of the liquid density branch. At higher surface–fluid attraction, $\varepsilon_{wf} = 4$, a monotonic decreasing trend in critical temperature and an increasing trend in critical density is observed for the studied system, as shown in Figure 2(c). This is due to the pronounced shifting of the vapour

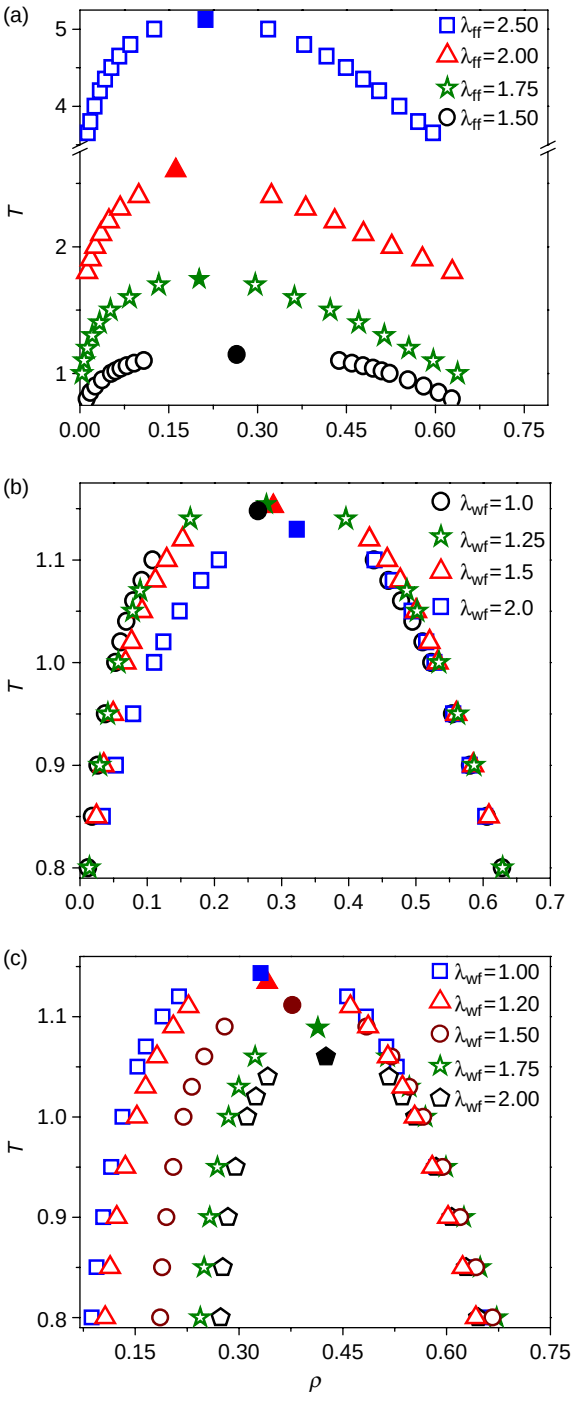

Figure 2. Vapour–liquid phase coexistence envelope and critical properties of SW fluid in an ordered stripe slit pore: (a) different fluid–fluid interaction ranges (λ_{ff}) with fixed remaining interaction parameters ($\lambda_{wf} = 1.0$, $\varepsilon_{wf} = 2.0$, $\varepsilon_{ff} = 1.0$); (b) different wall–fluid interaction ranges (λ_{wf}) with fixed remaining interaction parameters ($\lambda_{ff} = 1.5$, $\varepsilon_{ff} = 1.0$, $\varepsilon_{wf} = 2.0$); (c) stronger wall–fluid interaction ($\varepsilon_{wf} = 4.0$) with remaining parameters same as in (b). Filled symbols represent critical points. Error bars are of the order of the symbol size.

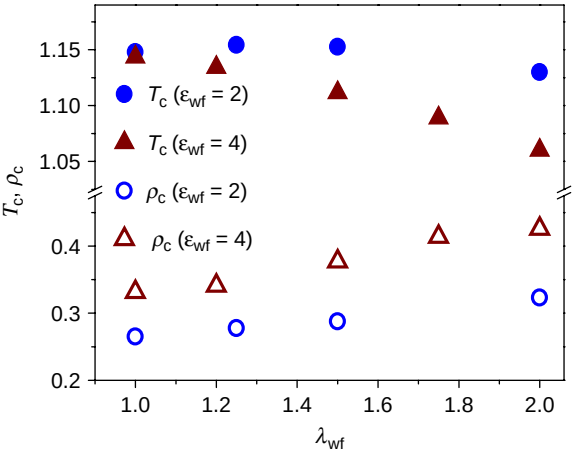

Figure 3. Critical temperature and critical density vs. wall–fluid interaction range is shown for the two cases (b) and (c) of Figure 2. Stripe width, w, and slit width, H, are kept fixed at 2 and 8 molecular diameters, respectively. Error bars are of the order of the symbol size.

density branch towards higher values. In addition, it is also observed that shifting of the vapour density branch towards higher values with the increase in the surface attraction range, λ_{wf}, is not linear. Figure 3 shows more precisely the trends of the critical properties with the increasing λ_{wf} from 1.0 to 2.0, keeping other parameters, $w = 2$ and $H = 8$, fixed. The effect of λ_{wf} on the decrease in T_c and increase in ρ_c becomes more pronounced at higher ε_{wf}. For example, for, $\varepsilon_{wf} = 2$, critical temperature decreases only around 1.6%, whereas for $\varepsilon_{wf} = 4$, the decrease is around 7.3% for the same increase in the λ_{wf} from 1.0 to 2.0. The reason for this behaviour is the comparatively larger increase in the vapour densities with the increase in λ_{wf} as shown in Figure 2(c).

Figure 4(a) presents a comparison of spreading pressures for various λ_{ff} in the patterned geometry. Corresponding reduced bulk saturation pressures are also included for the comparative study. Reduced saturation pressures of SW fluids with variable well widths coincide with each other for the bulk fluid. On the other hand, under confinement of the patterned slit pore, corresponding state plots of pressure is seen to have interesting behaviour. Reduced saturation pressure (or spreading pressure in the current case) of the confined fluid with $\lambda_{ff} = 1.5$ is very close to the corresponding bulk P/P_c, with a slight deviation at higher temperature. As the fluid–fluid interaction is increased, significant deviation from the bulk values is seen. Interestingly, spreading pressures approximately coincide with each other for $\lambda_{ff} \geqq 2.0$, as shown in Figure 4(a), which indicates that after a certain range of λ_{ff}, the corresponding state behaviour is insensitive to the change in λ_{ff}. Figure 4(b) presents the effect of λ_{wf} on the P/P_c as a

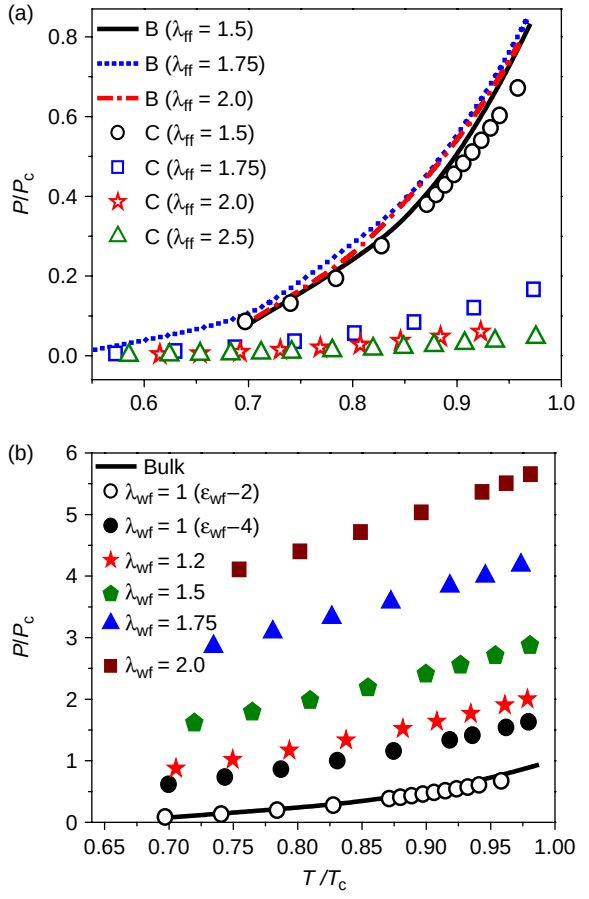

Figure 4. Reduced spreading pressure vs. reduced temperature of the SW fluid in an ordered stripe slit pore: (a) different fluid–fluid interaction ranges (λ_{ff}) with fixed remaining interaction parameters ($\lambda_{wf} = 1.0$, $\varepsilon_{wf} = 2.0$, $\varepsilon_{ff} = 1.0$); (b) different wall–fluid interaction ranges (λ_{wf}) with fixed remaining interaction parameters, $\lambda_{ff} = 1.5$, $\varepsilon_{ff} = 1.0$, $\varepsilon_{wf} = 4.0$ (solid symbols) and $\varepsilon_{wf} = 2.0$ (open symbol). Stripe width and slit width are kept fixed at 2 and 8, respectively. 'B' represents bulk fluid and 'C' represents confined fluid. Error bars are of the order of the symbol size.

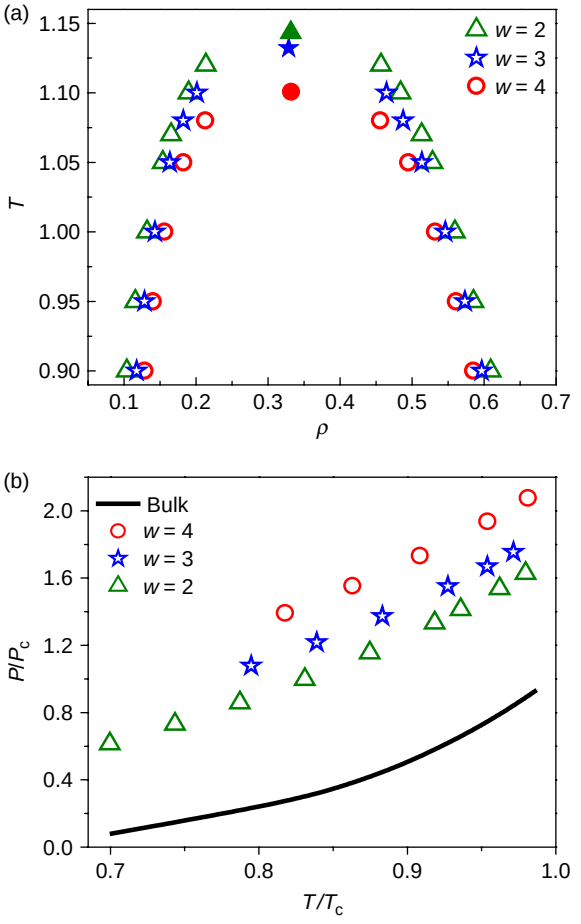

Figure 5. Vapour–liquid phase coexistence envelopes of a SW fluid in an ordered stripe slit pore with $H = 8$ and various stripe widths, w, are shown in (a). Filled symbols represent critical points. In (b), reduced spreading pressure vs. reduced temperature of the same SW fluid is shown. Continuous curve represents the bulk SW fluid. Other parameters $\lambda_{ff} = 1.5$, $\varepsilon_{ff} = 1.0$, $\lambda_{wf} = 1.0$, $\varepsilon_{wf} = 4.0$ are kept constant for both the cases (a) and (b). Error bars are of the order of the symbol size.

function of reduced temperature. Our investigations indicate that with smaller $\lambda_{wf} = 1.0$ and $\varepsilon_{wf} = 2$, the reduced spreading pressure coincides with the reduced bulk saturation pressures. However, as the wall–fluid interaction increases, $\varepsilon_{wf} = 4$, behaviour changes significantly. For example, at the fixed $\lambda_{wf} = 1.0$, with the increasing ε_{wf} from 2 to 4, spreading pressure increases significantly. Figure 4(b) also reveals that at a fixed $\varepsilon_{wf} = 4.0$, with the increase in the λ_{wf}, P/P_c monotonically increases for the range of temperatures investigated in this work. This behaviour is attributed to the relatively larger increase in vapour density, with increasing λ_{wf}, compared to that in liquid phase densities (see Figure 2(c)), which in turn resulted in the increased spreading pressure.

Our investigation of the phase coexistence envelope for three different stripe widths, namely $w = 2$, 3 and 4 as shown in Figure 5(a), indicates that critical temperature decreases with increasing w but critical density remains almost the same. Total fractional areas of the attractive interaction of all the aforementioned stripe width cases are the same. It is obvious, from Figure 5(a), that with increasing w, phase coexistence vapour densities shift towards a higher value, whereas phase coexistence liquid densities shift towards a lower value, which in turn resulted in the decrease in the difference of liquid–vapour density and hence decrease in critical temperature. On the other hand, critical density depends on the density diameters, $(\rho_v + \rho_l)/2$, which in fact remains almost constant, hence critical density is unaffected by the change in w for the investigated patterned slit pores. Our investigations indicate that for a fixed H, with the increase in w, reduced spreading pressure increases for the studied systems as

shown in Figure 5(b). The reason for this behaviour can be explained from the phase coexistence envelope observed in Figure 5(a), which indicates that with the increase in w, vapour density relatively increases, which resulted in the increase in reduced spreading pressure.

We further investigated structural properties through density profile calculations. Figures 6(a) and (b) show the phase coexistence liquid and vapour density profiles in the X direction for $\lambda_{ff} = 1.5$, $\varepsilon_{ff} = 1.0$; $\lambda_{wf} = 1.0$, $\varepsilon_{wf} = 2.0$ at $T = 1.0$. It is observed that on the attractive region, density is higher compared to that on the inert region for both the liquid and vapour phases as particles tend to adsorb more on the attractive region. This behaviour is similar to that seen by previous workers [23]. In Figure 6(a), for stripe widths, $w = 1$ and 2, we obtain two peaks for each stripe; whereas for $w = 3$, there are three peaks for each stripe. Moreover, the magnitude of peaks decreases with increasing w from 1 to 3. On the attractive surfaces for $w = 1$ and 2, molecules accumulate in two layers perpendicular to the surface (i.e. in the Z-direction). Two peaks for $w = 1$ near the edge suggest maximum packing of particles on the attractive region. With increasing w from 1 to 3, the third layer is seen to emerge. For all the cases, the density is maximum at the edge of the attractive stripes. Density behaviour in the vapour phase is slightly different as shown in Figure 6(b). Particles are seen to accumulate near the edge similar to the behaviour seen in the liquid phase. However, this accumulation is uniform across the stripe for $w = 2$. Subsequently, the increase in w led to the depletion of particles from the edge of the stripe and an accumulation in the middle of the stripe is seen. The behaviour is completely opposite for hard stripe regions as shown in Figure 6(b). The liquid density profile in the Z-direction, as shown in Figure 6(c), shows an ordered and higher density structure near the surfaces, because of the attractive nature of the stripe surfaces. For the vapour phase, the layering near the slit surfaces is more prominent as shown in Figure 6(d); moreover, with the increase in w, the Z-density of the liquid phase layers remains almost constant but the density of the vapour phase layers increases with w, which is more prominent near the slit surfaces.

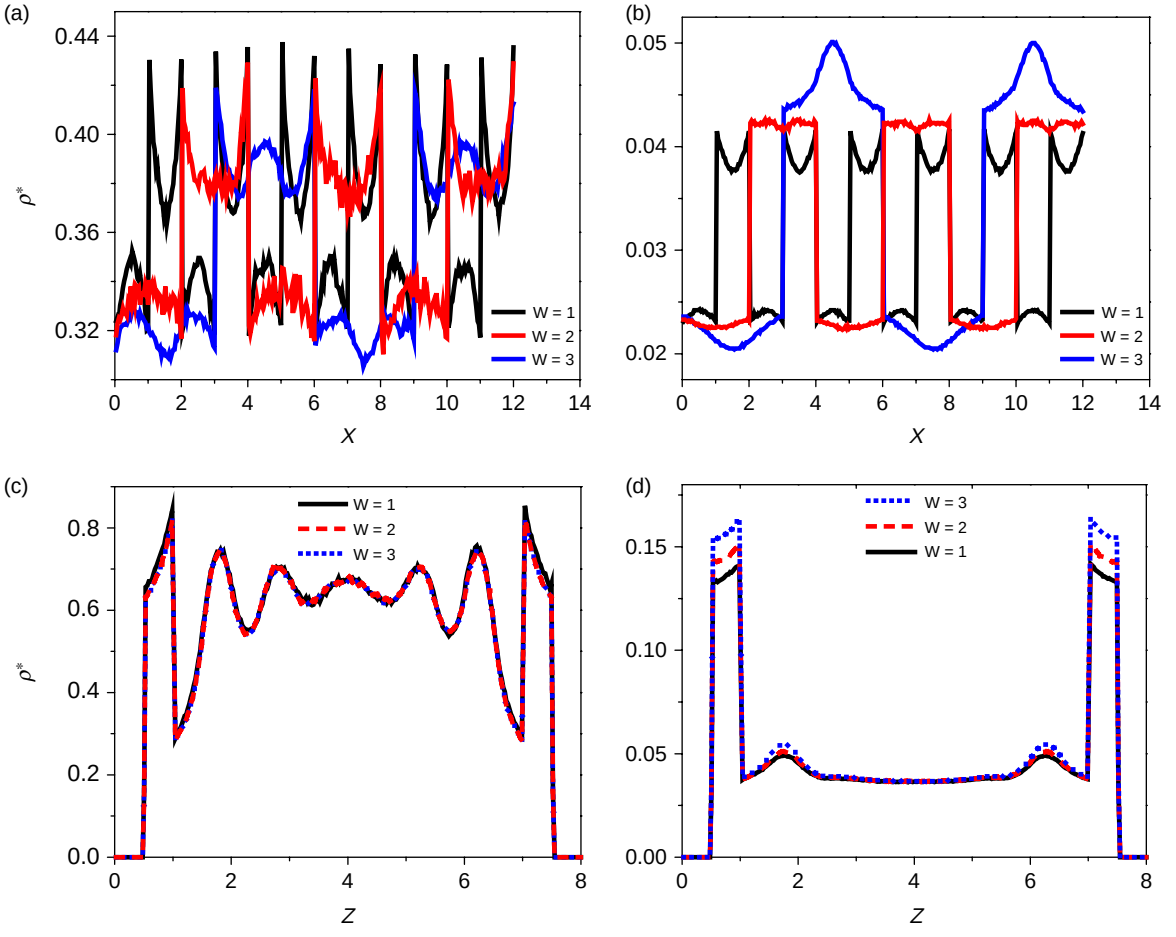

Figure 6. Density profiles in the slit pore at $T = 1.0$ with SW parameters ($\lambda_{ff} = 1.5$, $\varepsilon_{ff} = 1.0$, $\lambda_{wf} = 1.0$, $\varepsilon_{wf} = 2.0$) at various stripe widths ($w = 1$, 2 and 3), and fixed surface area $A = 144$ and $H = 8$. (a) and (b) represent the X-density profiles of the liquid and vapour phases, respectively; (c) and (d) are Z-density profiles of the liquid and vapour phases, respectively.

3.2 Phase equilibria in physically patterned pores

It is expected that physical patterning in the slit pore geometry of attractive surfaces will affect the vapour–liquid phase equilibria of the system. To this end, we have carried out a detailed investigation of the vapour–liquid phase equilibria by taking a typical case of the slit width $H = 8$. Here, we present a systematic study of the vapour–liquid phase equilibria of a SW fluid in physically patterned slit pores of various pillar widths, w, pillar gaps, g, and pillar heights, h.

Figure 7(a) presents a typical 2D schematic of a physically patterned slit pore used in the current work. In Figure 7(b), the particle number probability distribution is shown for a typical case, $w = 2$, $g = 2$ and $h = 2$ at $T = 0.98$ for the patterned slit pore with $H = 8$. Snapshots shown in Figure 7(b), corresponding to the probability distribution peaks, represent the vapour and liquid phases in the physically patterned slit pore geometry. Figure 8 shows the vapour–liquid phase diagram for various w, g and h for an attractive slit pore with $\varepsilon_{wf} = 2.0$, $\lambda_{ff} = 1.5$, $\varepsilon_{ff} = 1.0$ and $\lambda_{wf} = 1.0$. We have done similar studies with higher surface attraction, $\varepsilon_{wf} = 4.0$, but except for the case with $w = 2$, $g = 2$ and $h = 2$, we observed the existence of some metastable phases of intermediate densities between the vapour and liquid phases. Our investigations, as shown in Figure 8, indicate that changing the pillar width w, keeping g and h fixed along with the fixed model parameters as reported above, has an insignificant effect on the vapour–liquid phase equilibria. For example, by increasing w from 1 to 3, T_c, ρ_c and P_c decrease by 0.8, 1.9 and 2%, respectively, for the fixed $g = 1$ and $h = 1$. Similar is the case for other combinations of w, g and h. On the other hand, by changing the pillar height h, we observed a significant change in the vapour–liquid phase equilibria. For example, with w and $g = 1$ and by changing h from 1 to 2, T_c, ρ_c and P_c decrease by ~7.4, 24.8 and 28.9%, respectively. Similarly, with w and $g = 2$ and by changing h from 1 to 3, T_c, ρ_c and P_c decrease by ~23.5, 24.6 and 47.6%, respectively; and by changing h from 1 to 3, for $w = 3$ and $g = 1$, T_c, ρ_c and P_c decrease around 33.2, 36.2 and 72.2%, respectively. This indicates that the pillar height affects the critical properties significantly. Interestingly, equal values of w and $g = 2$ has shown lesser decrement in critical properties as compared to the case with $w = 3$ and $g = 1$, for the same change in pillar height, h, from 1 to 3. This suggests that the greater the physical heterogeneity, the higher the effect on the phase equilibria and, hence, in the critical properties as shown in Figure 8. Moreover, we have also studied the effect of the pillar gap, g, on the vapour–liquid phase equilibria. Our investigations indicate that with the fixed w and $h = 2$, by increasing g from 1 to 3, T_c, ρ_c and P_c increase around 4.5, 7.4 and 22.2%, respectively.

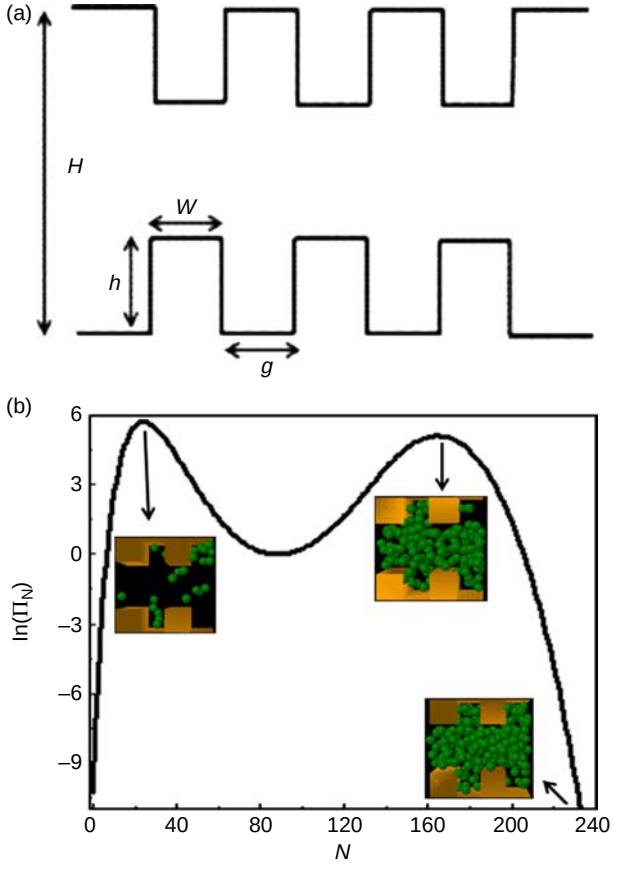

Figure 7. Schematic diagram for a physically patterned slit pore is shown in (a). w, g and h represent pillar width, gap and height, respectively; H represents the maximum slit width. In (b), particle number probability distribution, $\ln(\Pi_N)$, for a typical case, $w = 2$, $g = 2$, $h = 2$ at $T = 0.98$, is shown. Snapshots shown in (b) represent a few typical vapour and liquid configurations.

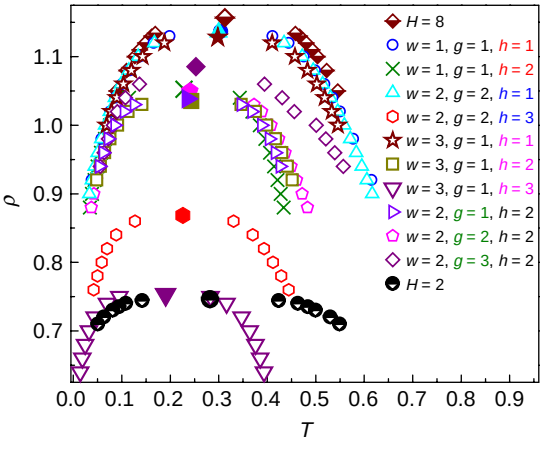

Figure 8. Vapour–liquid phase coexistence envelopes of a SW fluid in a physically patterned slit pore, with $H = 8$, for various w, g and h. Half-filled symbols represent the phase diagram of a homogeneous attractive slit pore with slit width $H = 8$ and 2. Filled symbols represent the critical points of the various physically patterned slit pores. Model parameters $\lambda_{ff} = 1.5$, $\varepsilon_{ff} = 1.0$, $\lambda_{wf} = 1.0$ and $\varepsilon_{wf} = 2.0$ are kept constant for all the studied cases. Error bars are of the order of the symbol size.

This indicates that comparative changes in critical properties are less prominent for a unit change in g as compared to the change in h.

Figure 9 compares the local density profiles of the vapour and liquid phases for the two typical cases of $w = 1$ and 3, keeping fixed $T = 1.02$, $H = 8$, $g = 1$ and $h = 2$. In Figure 9(a), local X-density profiles of the vapour and liquid phases are shown for the case of $X = 12$. It is observed that at a larger pillar width, $w = 3$, in the middle region of the pillar width, a local peak is observed both in the liquid and vapour phases; however, at $w = 1$, particles tend to minimise the energy of the configuration by packing densely within the pillar region. Such reorganisation of particles increases the density near the edge of the pillar relative to other regions of the pore. Similar behaviour is also noticed for the pillar width $w = 3$. However, local liquid density at the pillar width edges of $w = 1$ is larger compared to that seen for $w = 3$; on the other hand, the reverse is observed for the local vapour phase density. In the pillar gap regime, g, local X-density of the vapour phase is almost the same for both the cases of pillar widths, $w = 1$ and 3; however, liquid density for the case of smaller w is comparatively larger. In Figure 9(b), corresponding Z-density profiles of the vapour and liquid phases are shown. Qualitatively, the nature of the vapour and liquid phase profiles are the same for both the cases of w. However, in the Z-direction up to the pillar height h, from either side of the surfaces, or more precisely for $Z \leq 2.5$ or $Z \geq 5.5$, liquid density with $w = 1$ comparatively dominates over that of $w = 3$. Moreover, away from h, i.e. in the remaining pore region, $2.5 < Z < 5.5$, liquid profiles fluctuate in a periodic manner for the studied cases of w. Similarly, the vapour profiles with $w = 1$ comparatively dominates over that of $w = 3$, for $Z \leq 2.5$ or $Z \geqq 5.5$; however, contrary to the fluctuating behaviour of the liquid density profile, the vapour profile in the pore regions, $2.5 < Z < 5.5$, with $w = 3$ comparatively dominates over that of $w = 1$.

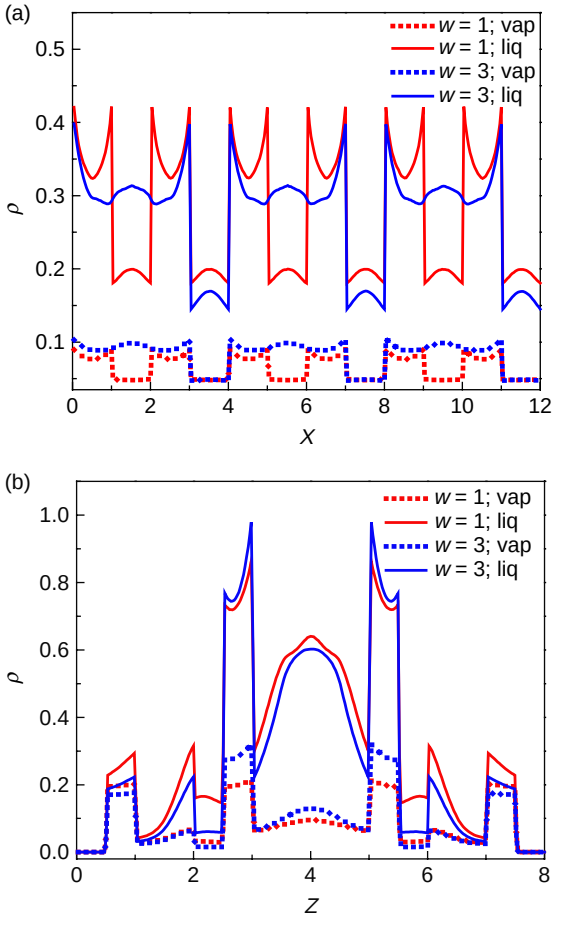

Figure 9. Local X-density and Z-density profiles of the vapour and liquid phases for a fixed $T = 1.02$, $H = 8$, $g = 1$ and $h = 2$ are shown in (a) and (b), respectively, for two typical cases of pillar width, w. Model parameters are kept constant for all the studied cases and are same as in Figure 8.

In Figure 10, the local X-density and Z-density profiles of the vapour and liquid phases are compared for two typical cases of pillar gaps, $g = 1$ and 2, for a fixed $T = 1.0$, $H = 8$, $w = 2$ and $h = 2$. Figure 10(a) shows that at the edges of the pillar width, local X-densities of the liquid phase are maximum as also observed with the previous case as well. Moreover, the liquid densities at the edge of the pillar of larger gaps are comparatively higher. Also, for both the studied cases, $g = 1$ and 2, in the middle of the pillar gap, the local liquid density peak is observed, with higher density for larger gap. On the other hand, the vapour phase X-density profile has shown similar densities at the respective edges of the pillar width and pillar gap. In Figure 10(b), corresponding Z-density profiles of the vapour and liquid phases are shown. Qualitatively, the nature of the vapour and liquid phase profiles remains the same for both the cases of $g = 1$ and 2. However, in the Z-direction up to the pillar height h, from either side of the surfaces, i.e. with $Z \leq 2.5$ or $Z \geq 5.5$, liquid density with $g = 2$ is relatively higher than that with $g = 1$. Moreover, away from h, i.e. in the remaining pore regions, $2.5 < Z < 3$, and with $5 < Z < 5.5$, dominance of the liquid profile with $g = 1$ is observed. However, in the middle region of the slit pore, i.e. $3 < Z < 5$, the profile with $g = 2$ dominates over $g = 1$ for the studied cases of w and h. Similarly, vapour profiles with $g = 2$ dominates over that of $g = 1$, for $Z \leq 2.5$ or $Z \geq 5.5$; however, contrary to the fluctuating behaviour of the liquid density profile, the vapour profile in the pore regions, $2.5 < Z < 5.5$, with $g = 1$, has shown comparative dominance over that of $g = 2$.

In Figure 11, local X-density and Z-density profiles of the vapour and liquid phases are compared for two typical cases of pillar heights, $h = 1$ and 2, for a fixed $T = 1.0$, $H = 8$, $w = 3$ and $g = 1$. Figure 11(a) shows that at the edges of the pillar width, local X-densities of the liquid

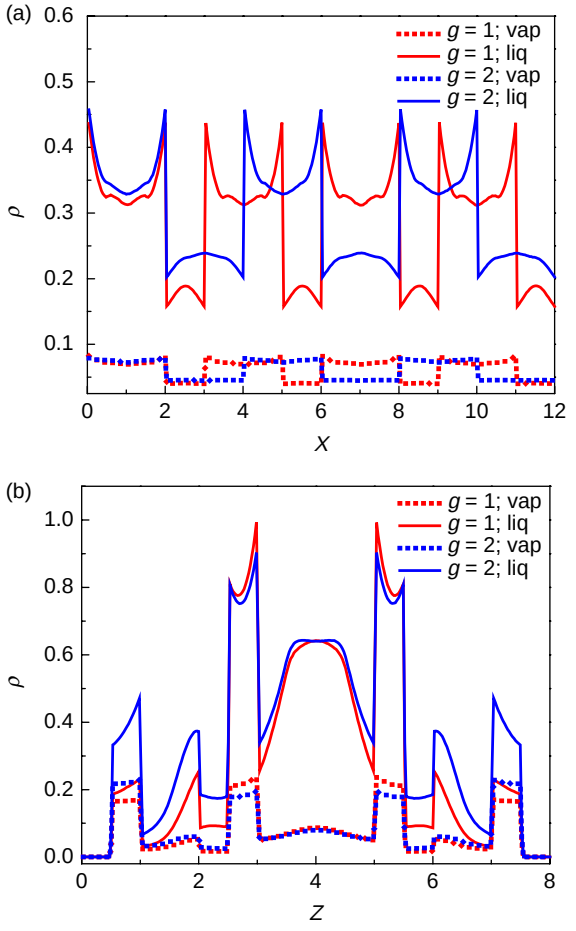

Figure 10. Local X-density and Z-density profiles of the vapour and liquid phases for a fixed $T = 1.0$, $H = 8$, $w = 2$ and $h = 2$ are shown in (a) and (b), respectively, for two typical cases of pillar gap, g. Model parameters are kept constant for all the studied cases and are same as in Figure 8.

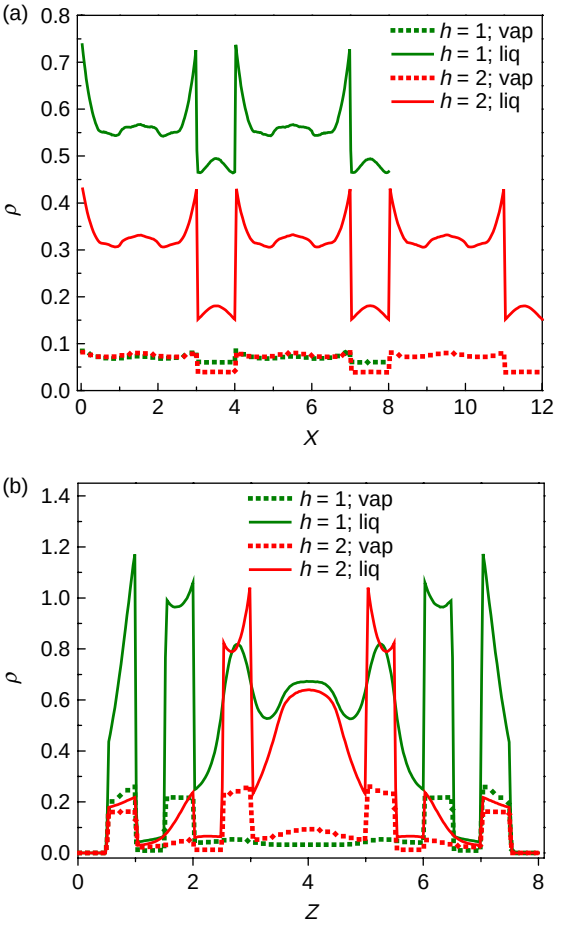

Figure 11. Local X-density and Z-density profiles of the vapour and liquid phases for a fixed $T = 1.0$, $H = 8$, $w = 3$ and $g = 1$ are shown in (a) and (b), respectively, for two typical cases of the pillar height h. Model parameters are kept constant for all the studied cases and are same as in Figure 8.

phase are maximum, also in the middle region of the pillar width or pillar gap, a peak is observed irrespective of the pillar height h. Moreover, the qualitative nature of the liquid profiles remains unaffected by the pillar heights studied in this work. However, quantitatively, the local X-liquid density profile, for $h = 1$, has shown continuous dominance over $h = 2$, as expected. On the other hand, the local X-density profile of the vapour phase reveals insignificant difference qualitatively as well as quantitatively in the regime of the pillar width w. However, in the regime of the pillar gap, g, the local vapour density profile with smaller pillar height, $h = 1$, dominates over larger pillar height of $h = 2$. Figure 11(b) shows the corresponding local Z-density profiles. It is observed that the local Z-liquid density profile for $h = 1$ dominates over $h = 2$ in the majority of the pore regimes except in the regime of $2.5 < Z < 3$ and $5 < Z < 5.5$, where the local Z-density of $h = 2$ dominates. Similarly, the vapour phase local Z-density profile with $h = 1$ dominates over $h = 2$, for the regime $0.5 < Z < 2.5$ and $5.5 < Z < 7.5$. However, in the middle region of the slit pore, i.e. $2.5 < Z < 5.5$, the local Z-vapour density is higher for the case of pillar height $h = 2$ compared to that for $h = 1$.

4. Conclusions

We have determined the phase behaviour of the vapour–liquid phases of SW fluids confined between chemically and physically patterned slit surfaces using the GC-TMMC simulation technique. Our investigations in a chemically patterned slit pore of alternating attractive and inert rectangular patches of a semi-infinitely large dimension with a unit ratio of attractive to inert surface area indicate that critical temperature is insensitive to the chemical pattering of inert and attractive stripes, as compared to the attractive homogeneous slit surfaces; however, critical density shows a comparatively significant effect and increases with chemically patterned slit

pore. In the chemically patterned slit pore, with the increase in the fluid–fluid attraction range, critical temperature monotonically increases, as expected; however, critical density first decreases to a minima and then increases. On the other hand, with the increase in the fluid–surface attraction range, critical temperature decreases monotonically, which is accentuated at higher fluid–surface attraction strength. Our investigations with a fixed slit width, H, and various stripe widths indicate that with the increase in the stripe width (keeping the same fractional area of attractive to inert stripe), critical density remains almost unchanged, whereas critical temperature decreases monotonically for the studied stripe widths. Various interesting trends of spreading pressure are observed with the change in the fluid and surface attraction range parameters. Moreover, structural properties of the fluid were revealed through local density profiles of the two coexisting phases in the chemically patterned slit pores of various stripe widths.

We have also investigated the effect of physical patterning on the vapour–liquid phase equilibria and critical properties of the confined fluid. Our investigations indicate that change in w at the fixed g and h has an insignificant effect on the coexisting vapour and liquid densities and hence critical properties ($<2\%$). However, for a fixed w and g, change in h, and for a fixed w and h, change in g has shown significant changes in the phase coexistence densities and the critical properties. Interestingly, for the same change in h, uneven spatial heterogeneity (i.e. $w \neq g$) resulted in greater change in vapour–liquid phase coexistence envelope and critical properties as compared to the even spatial heterogeneity (i.e. $w = g$). This indicates that spatial heterogeneity induced by physical patterning yielded a significant structural changes in the coexisting fluid phases, as revealed by the local density profiles.

Acknowledgements

This work was supported by the Department of Science and Technology, Government of India (Grant No. IR/S3/EU/005/2007).

References

[1] D.W.L. Tolfree, *Microfabrication using synchrotron radiation*, Rep. Prog. Phys. 61 (1998), pp. 313–351.

[2] B.F. Burmeister, C. Schafle, B. Keilhofer, C. Bechinger, J. Boneberg, and P. Leiderer, *From mesoscopic to nanoscopic surface structures: Lithography with colloid monolayers*, Adv. Mater. 10 (1998), pp. 495–497.

[3] P. Zeppenfeld, V. Diercks, R. David, F. Picaud, C. Ramseyer, and C. Girardet, *Selective adsorption and structure formation of N_2 on the nanostructured Cu–CuO stripe phase*, Phys. Rev. B 66 (2002), pp. 85414–85425.

[4] C. Schäfle, C. Bechinger, B. Rinn, C. David, and P. Leiderer, *Cooperative evaporation in ordered arrays of volatile droplets*, Phys. Rev. Lett. 83 (1999), pp. 5302–5305.

[5] P. Lenz, C. Bechinger, C. Schafle, P. Leiderer, and R. Lipowsky, *Perforated wetting layers from periodic patterns of lyophobic surface domains*, Langmuir 17 (2001), pp. 7814–7822.

[6] S. Harkema, E. Schaffer, M.D. Morariu, and U. Steiner, *Pattern replication by confined dewetting*, Langmuir 19 (2003), pp. 9714–9718.

[7] D. Öner and T.J. Mccarthy, *Ultrahydrophobic surfaces. Effects of topography length scales on wettability*, Langmuir 16 (2000), pp. 7777–7782.

[8] S.O. Kim, H.H. Solak, M.P. Stoykovich, N.J. Ferrier, J.J. De Pablo, and P.F. Nealey, *Epitaxial self-assembly of block copolymers on lithographically defined nanopatterned substrates*, Nature 424 (2003), pp. 411–414.

[9] R. Ruiz, H. Kang, F.A. Detcheverry, E. Dobisz, D.S. Kercher, T.R. Albrecht, J.J. De Pablo, and P.F. Nealey, *Density multiplication and improved lithography by directed block copolymer assembly*, Science 321 (2008), pp. 936–939.

[10] A. Pallandre, B. De Meersman, F. Blondeau, B. Nysten, and A.M. Jonas, *Tuning the orientation of an antigen by adsorption onto nanostriped templates*, J. Am. Chem. Soc. 127 (2005), pp. 4320–4325.

[11] H. Agheli, J. Malmström, E.M. Larsson, M. Textor, and D.S. Sutherland, *Large area protein nanopatterning for biological applications*, Nano Lett. 6 (2006), pp. 1165–1171.

[12] S. Lei, C. Wang, L. Wan, and C. Bai, *Site selective adsorption and templated assembling: Effects of organic–organic heterogeneous interface studied by scanning tunneling microscopy*, J. Phys. Chem. B 108 (2004), pp. 1173–1175.

[13] F. Shi, Z. Wang, N. Zhao, and X. Zhang, *Patterned polyelectrolyte multilayer: Surface modification for enhancing selective adsorption*, Langmuir 21 (2005), pp. 1599–1602.

[14] M. Patra and P. Linse, *Simulation of grafted polymers on nanopatterned surfaces*, Nano Lett. 6 (2006), pp. 133–137.

[15] A. Striolo, *Adsorption of model surfactant-like copolymers on nanopatterned surfaces*, J. Chem. Phys. 125 (2006), pp. 94709–94718.

[16] H. Chen, C. Peng, Z. Ye, H. Liu, Y. Hu, and J. Jiang, *Recognition of multiblock copolymers on nanopatterned surfaces: Insight from molecular simulations*, Langmuir 23 (2007), pp. 2430–2436.

[17] M. Schoen and D.J. Diestler, *Liquid–vapor coexistence in a chemically heterogeneous slit-nanopore*, Chem. Phys. Lett. 270 (1997), pp. 339–344.

[18] J. Puibasset, *Capillary condensation in a geometrically and a chemically heterogeneous pore: A molecular simulation study*, J. Phys. Chem. B 109 (2005), pp. 4700–4706.

[19] J. Puibasset, *Phase coexistence in heterogeneous porous media: A new extension to Gibbs ensemble Monte Carlo simulation method*, J. Chem. Phys. 122 (2005), pp. 134710–134721.

[20] J. Puibasset, *Influence of surface chemical heterogeneities on adsorption/desorption hysteresis and coexistence diagram of metastable states within cylindrical pores*, J. Chem. Phys. 125 (2006), pp. 74707–74711.

[21] A. Vishnyakov, E.M. Piotrovskaya, E.N. Brodskaya, E.V. Votyakov, and Y.K. Tovbin, *Critical properties of Lennard-Jones fluids in narrow slit-shaped pores*, Langmuir 17 (2001), pp. 4451–4458.

[22] J. Jiang and S.I. Sandler, *Adsorption and phase transitions on nanoporous carbonaceous materials: Insights from molecular simulations*, Fluid Phase Equilibr. 228 (2005), pp. 189–195.

[23] H. Bock and M. Schoen, *Phase behavior of a simple fluid confined between chemically corrugated substrates*, Phys. Rev. E 59 (1999), pp. 4122–4136.

[24] J. Puibasset, *Adsorption/desorption hysteresis of simple fluids confined in realistic heterogeneous silica mesopores of micrometric length: A new analysis exploiting a multiscale Monte Carlo approach*, J. Chem. Phys. 127 (2007), pp. 154701–154711.

[25] J.K. Singh and S.K. Kwak, *Surface tension and vapor–liquid phase coexistence of confined square-well fluid*, J. Chem. Phys. 126 (2007), pp. 24702–24710.

[26] J.R. Errington, *Direct calculation of liquid–vapor phase equilibria from transition matrix Monte Carlo simulation*, J. Chem. Phys. 118 (2003), pp. 9915–9925.

[27] J.K. Singh, J. Adhikari, and S.K. Kwak, *Vapor–liquid phase coexistence curves for Morse fluids*, Fluid Phase Equilibr. 248 (2006), pp. 1–6.

[28] L.J. Van Poolen, C.D. Holcomb, and V.G. Niesen, *Critical temperature and density from liquid–vapor coexistence data: Application to refrigerants R32, R124, and R152a*, Fluid Phase Equilibr. 129 (1997), pp. 105–111.

[29] S.K. Singh, A. Sinha, G. Deo, and J.K. Singh, *Vapor–liquid phase coexistence, critical properties, and surface tension of confined alkanes*, J. Phys. Chem. C 113 (2009), pp. 7170–7180.

[30] A.M. Ferrenberg and R.H. Swendsen, *New Monte Carlo technique for studying phase transitions*, Phys. Rev. Lett. 61 (1988), pp. 2635–2638.

[31] S. Jana, J.K. Singh, and S.K. Kwak, *Vapor–liquid critical and interfacial properties of square-well fluids in slit pores*, J. Chem. Phys. 130 (2009), pp. 214707–214715.

[32] S.K. Singh, A. Saha, and J.K. Singh, *A molecular simulation study of vapor–liquid critical properties of a simple fluid in attractive slit pores: Crossover from 3D to 2D*, J. Phys. Chem. B 114(12) (2010), pp. 4283–4292.